the FEBS Journal

Intrinsic local disorder and a network of charge–charge interactions are key to actinoporin membrane disruption and cytotoxicity

Miguel A. Pardo-Cea[1,*], Inés Castrillo[1,*], Jorge Alegre-Cebollada[2,†], Álvaro Martínez-del-Pozo[2], José G. Gavilanes[2] and Marta Bruix[1]

1 Departamento de Química Física Biológica, Instituto de Química Física Rocasolano, Madrid, Spain
2 Departamento de Bioquímica y Biología Molecular I, Facultad de Química, Universidad Complutense, Madrid, Spain

Keywords
actinoporin; dynamics; electrostatic interactions; NMR structure; sticholysin

Correspondence
M. Bruix, Departamento de Química Física Biológica, Instituto de Química Física Rocasolano, CSIC, Serrano 119, 28006 Madrid, Spain
Fax: +34 91 561 9400
Tel: +34 91 745 9511
E-mail: mbruix@iqfr.csic.es

*These two authors contributed equally to this work

†**Present address**
Department of Biological Sciences, Columbia University, New York, USA

(Received 1 February 2011, revised 10 March 2011, accepted 1 April 2011)

doi:10.1111/j.1742-4658.2011.08123.x

Actinoporins are a family of sea anemone proteins that bind to membranes and produce functional pores which result in cell lysis. Actinoporin variants with decreased lytic activity usually show a reduced affinity for membranes. However, for some of these mutant versions there is no direct correlation between the loss of binding affinity and the decrease in their overall lytic activity, suggesting that other steps in pore formation may be hampered or facilitated by the mutations. To test this hypothesis on the mechanism of pore formation by this interesting family of proteins, structural and dynamic NMR studies have been carried out on two disabled variants of the actinoporin Sticholysin II, R29Q and Y111N. It is shown that their lytic activity is not only related to their membrane affinity but also to their conformational mechanism for membrane insertion. Alterations in their activities can be explained by structural, electrostatic and dynamic differences in a cluster of aromatic moieties and the N-terminus. In addition, the dynamic properties of some segments located at the C-terminus of the R29Q variant suggest a relevant role for this region in terms of protein–protein interactions. On the basis of all these results, we propose that R29 anchors a network of electrostatic interactions crucial for the actinoporin's approach to the membrane and that Y111 induces a necessary disorder in the loop regions that bind to membranes.

Introduction

Actinoporins are very potent cytolysins secreted as part of the venom of a large number of sea anemones [1]. These proteins are produced as water-soluble monomers that form oligomeric pores upon interaction with membranes [2–5]. Sticholysin II (StnII) is an actinoporin isolated from the Caribbean species *Stichodactyla helianthus*. The three-dimensional structure of the soluble form of StnII [6], as well as that of its relative Equinatoxin II from *Actinia equina* [7,8], have been solved. Both proteins share the same global tertiary structure composed of a β-barrel flanked by two short α-helices, one at each side (Fig. 1). Studies performed in recent years have made it possible to propose a model for the interaction of these proteins with cellular

Abbreviations
POC, phosphocholine; StnII, Sticholysin II.

membranes [9–11] including the pore formation mechanism [3,12–14]. First, a cluster of aromatic residues and a phosphocholine (POC) binding site, together with some positively charged side chains, would be responsible for the initial attachment to the membrane. Then, the N-terminal region would extend the α-helix and penetrate into the membrane, forming the pore. However, the molecular bases directing these processes are still largely unknown. In this regard, mutagenesis studies have proved to be very useful to detect the implication of certain regions of StnII in the different steps involved in the formation of the pore [15,16]. In particular, calorimetric and other structural and spectroscopic studies on StnII suggested that residues at positions 29 (Arg) and 111 (Tyr), which are 100% conserved in the actinoporins family [17,18], have an important functional role in membrane binding [16]. R29 is located in the protein segment that is supposed to rotate in the first steps of pore formation. Additionally, R29 belongs to one cluster of cationic residues that has been postulated as an important motif due to its situation between the N-terminus and the other binding regions of StnII. Also, Y111 is crucial for membrane binding as it is located at the POC binding site.

It was shown previously [16] that the two mutations R29Q and Y111N have an identical effect on membrane binding: they lower it to 13% of that of the wild-type protein. Although the lytic activity is much reduced for both variants, it is particularly small for the Y111N. In fact, the lytic activity is five times lower for Y111N than for R29Q. Taken together, on the basis of these previously reported data, we now hypothesize that actinoporins act in at least two stages: (a) an initial approach to and binding of the membrane; (b) oligomerization, pore formation and lysis. We also hypothesize that R29 and Y111 contribute distinctly to the second stage.

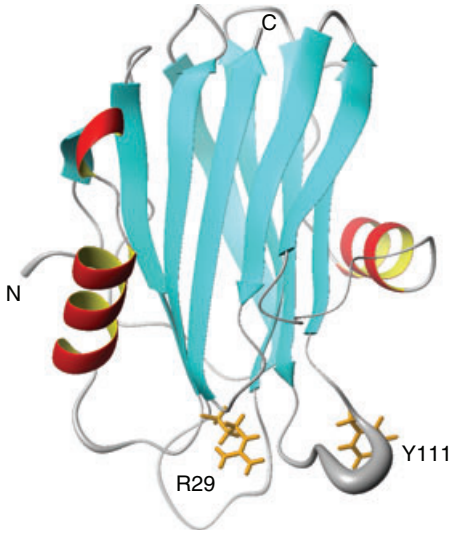

Fig. 1. Crystal structure of wild-type StnII. The thickness of the backbone trace is proportional to the reported B-factors (pdb:1gwy). The secondary structure elements and the side chains of R29 and Y111 are shown. The figure was created with MOLMOL [29].

In this work, NMR spectroscopy has been used to determine the solution structure and dynamics of the StnII-R29Q and StnII-Y111N variants. Structurally, both substitutions are moderately conservative. The glutamine side chain, despite its lack of positive charge, maintains the polar character and the possibility of donating H-bonds. In the Y111N variant, the aromatic ring is replaced by a group which is also structurally planar and able to accept and donate H-bonds. In this context, our data indicate that the positive surface together with a network of electrostatic interactions, and the presence of flexibility in the loops in close contact with the membranes, can play critical roles in the overall toxic mechanism of StnII. These results are relevant not only for the characterization of the molecular interactions of StnII with the membrane at residue level, but also to better understand the cytotoxic mechanism of this family of proteins.

Results

Global fold of StnII-R29Q and StnII-Y111N mutants

Figure 2 shows the three-dimensional structure of the two mutants in solution determined on the basis of the NMR restraints summarized in Table 1. The resulting structures satisfy the experimental constraints with small deviations from the idealized covalent geometry and most of the backbone torsion angles lie within the allowed regions in the Ramachandran plot. The global averaged pairwise rmsd values of the calculated 20 structures for the backbone were larger for StnII-R29Q (1.5 Å) than for StnII-Y111N (0.8 Å). However, when only the regular secondary elements were considered these values dropped to 0.7 and 0.6 Å, respectively, showing that these regions, which constitute the protein core, are similarly well defined. The global fold closely resembles that of wild-type StnII (Fig. 1) and the other proteins belonging to the actinoporins family [6–9].

Structure and dynamic properties of StnII-R29Q

The secondary structure of StnII-R29Q is composed of two α-helices (residues 14–22 and 128–135) and nine

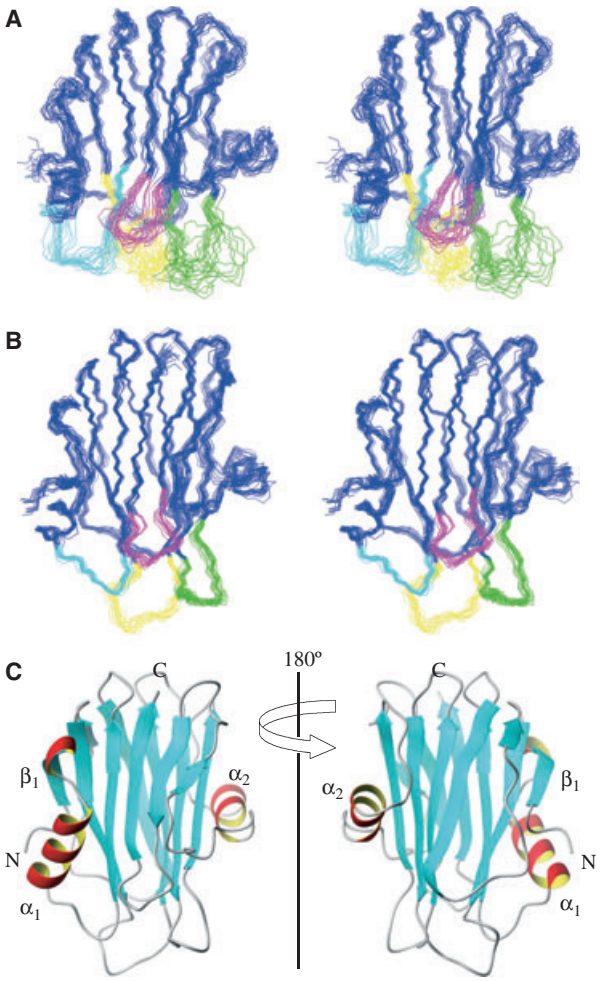

Fig. 2. Solution structure of the StnII-R29Q and StnII-Y111N mutants. The ensemble of the 20 final structures of StnII-R29Q (A) and StnII-Y111N (B) are shown as cross-eyed stereo diagrams with the mutated face pointing down. Loops corresponding to this face are represented in different colours: StnII-R29Q 23–32, cyan; 72–84, yellow; 103–113, green; 162–168, pink; StnII-Y11N 25–29, cyan; 75–83, yellow; 105–113, green; 161–167, pink. Two views rotated 180° of the ribbon diagram of the minimal energy structure of StnII-Y111N are shown in (C). The orientation of the structures in (A) and (B) is the same as in the left panel of (C). Some interesting regions and secondary structure units are indicated in (C). These figures were produced using MOLMOL [29].

β strands (33–38, 43–52, 67–71, 85–92, 96–102, 114–121, 145–150, 156–161 and 169–174) arranged according to the classical β-sheet actinoporin structural topology (Figs 1–3). Structural variability was only observed in segments corresponding to the loops connecting these regular secondary elements (Figs 2 and 3). This is especially evident for loops 23–32 (Fig. 2, cyan), 72–84 (Fig. 2, yellow), 103–113 (Fig. 2, green) and 162–168 (Fig. 2, pink) which have higher than average rmsd values. All these loops are topologically located in the same region of the protein which also corresponds to the membrane interaction face (Figs 2 and 4). In the wild-type structure, the side chain of R29 interacts with K75, T82, F106 and E166; thus it links together four different loops of the structure (Fig. 5). Mutation of this arginine residue by the shorter and neutral glutamine prevents the formation of those contacts and the loops are far apart in the R29Q mutant. As a consequence, F106 is more exposed to the solvent and loop 72–84 is disordered and adopts different conformations (Fig. 5). Furthermore, charge density on the side facing the membrane is dramatically changed (Fig. 4).

Finally, as ^{15}N NMR relaxation can be used to characterize the dynamic properties of a protein in solution, relaxation data were obtained for 147 of the 175 residues present in StnII-R29Q. It is interesting that signals from residues 29, 30, 106–107, 110–113 and 164–167 were not observable in the ^{15}N-HSQC spectra because of excessive broadening, most probably due to conformational exchange processes (Fig. 3). Good correlations could be established between structure and experimental relaxation data in that most residues in regular secondary structure elements exhibited heteronuclear NOE values close to the theoretical maximum, indicating high rigidity in these regions. In contrast, residues at the N- and C-termini, and in loop regions, showed decreased longitudinal relaxation rates (R_1), variable transversal relaxation rates (R_2) and low NOE values, suggesting a much higher mobility on the picoseconds time scale (Fig. 3).

Residues in loops exhibited decreased R_1 values indicating higher flexibility, but the overall differences are not significant (mean values 1.0 s^{-1}). More variability was clearly observed in the NOE and R_2 data, with mean values of 0.8 and 17.6 s^{-1}, respectively. Low R_2 values correlate with a decrease in the NOE ratio in loop 23–32, the first residues of loop 72–84 and position 111 (Fig. 3). However, other regions of StnII-R29Q with low or average NOE values present higher R_2 values with respect to the mean. These correspond to residues 82–84 and 104 in the membrane interaction face and segments 140–147 and 159–163 towards the end of the protein sequence (Fig. 3), indicating that these residues are affected by conformational exchange processes.

Structure and dynamic properties of StnII-Y111N

The secondary structure for variant Y111N is also well defined with two α-helices (residues 14–24 and 129–135) and nine β strands (30–37, 43–52, 67–74, 84–91,

Table 1. NMR structural calculations summary and statistics.

	StnII-R29Q		StnII-Y111N	
Calculation				
Distance restraints	2195		1450	
Angular restraints	178		254	
Max violation (Å)	0.4		0.2	
CYANA (20 structures)				
Energy function (mean value)	0.94 ± 0.42		0.67 ± 0.14	
AMBER (20 structures)				
Total energy (kcal·mol^{-1})	−5640 (−5718 to −5529)		−6015 (−6089 to −5930)	
van der Waals (kcal·mol^{-1})	−1194 (−1231 to −1145)		−1298 (−1330 to −1266)	
Electrostatic (kcal·mol^{-1})	−11481 (−12346 to −10420)		−11161 (−11967 to −10409)	
rmsd (Å)				
All residues (backbone, heavy atoms)	1.5 ± 0.2	2.4 ± 0.2	0.8 ± 0.1	1.4 ± 0.1
Secondary (backbone, heavy atoms)	0.7 ± 0.1	1.4 ± 0.2	0.6 ± 0.1	1.3 ± 0.1
Ramachandran plot				
Most favoured (%)	73.9		79.1	
Allowed (%)	24		19.3	
Add. allowed (%)	1.5		1.4	
Disallowed (%)	0.5		0.2	

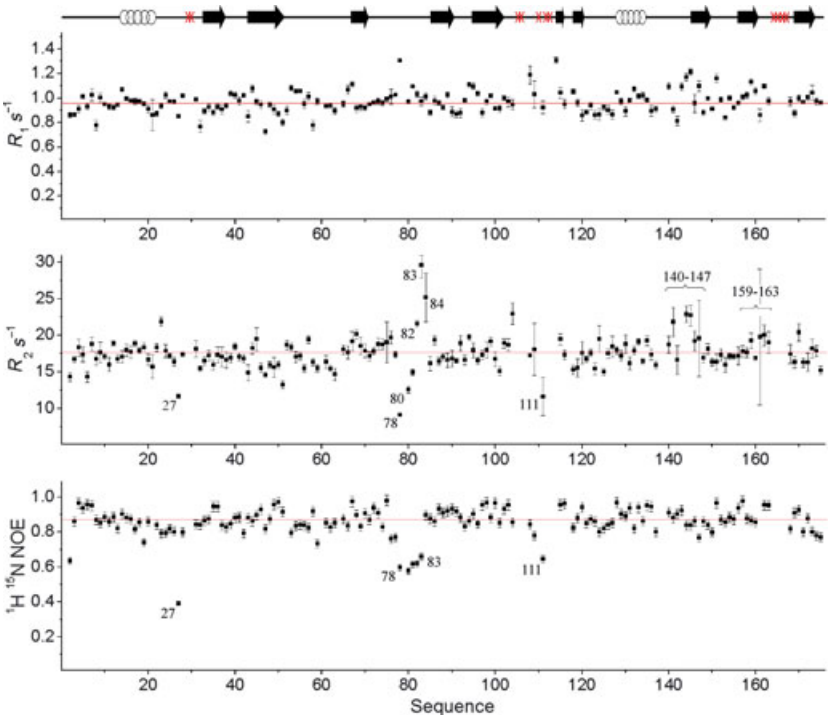

Fig. 3. Backbone NMR heteronuclear R_1 and R_2 relaxation rates and heteronuclear NOE data for StnII-R29Q as a function of the sequence (800 MHz, 25 °C and pH 4.0). The horizontal line represents the mean value and red crosses at positions 29, 30, 106–107, 110–113 and 164–167 represent missing NMR signals in the ^{15}N-HSQC spectrum because of excessive broadening.

97–104, 114–120, 147–148, 156–160 and 168–174) arranged in a β-barrel like those in the wild-type protein and StnII-R29Q mutant (Figs 1 and 2). In addition, the structure of StnII-Y111N shows two additional short β-strands (residues 5–8, 62–64) and a 3–10-helix (residues 9–11). Compared with wild-type StnII, a new hydrogen bond is detected between side chains of N111 and D107.

The substitution of Y111 for N provokes conformational changes in the surrounding structure (Fig. 6A).

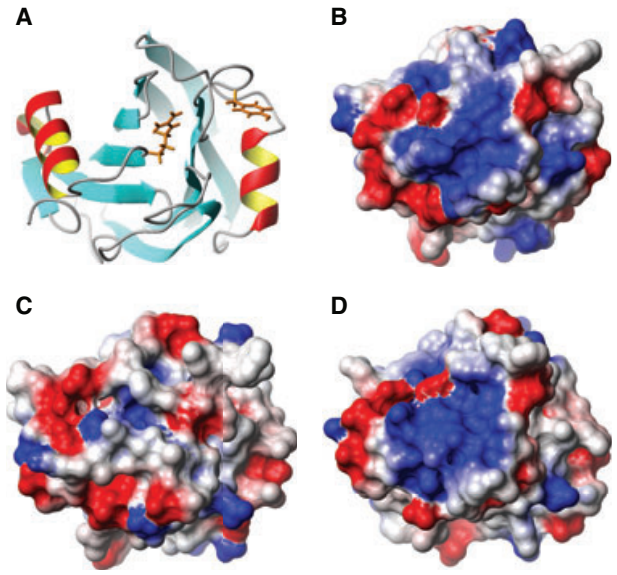

Fig. 4. Diagram showing the membrane interaction face of StnII (A) and its electrostatic distribution surface potential for the wild-type protein (B) and the StnII-R29Q (C) and StnII-Y111N (D) variants. Blue and red correspond to positively and negatively charged areas, respectively. The side chains of R29 and Y111 are shown in (A).

In particular, Y108 adopts a different conformation (Fig. 6B). Interestingly, helix-α_2 is slightly shifted while loops connecting it with the central β-barrel (121–128 and 136–146) are also structurally affected (Figs 1 and 6B). In addition, loops 25–29 and 75–83 adopt conformations that are slightly different from those found in wild-type StnII. Finally, the conformation of K26 side chain changes; it moves close to E166 and establishes a new electrostatic interaction not present in the parent protein. This interaction could cause the slightly different position of the above mentioned helix-α_2 and nearby areas (Fig. 6A).

Relaxation data were obtained for 153 residues in StnII-Y111N. The profiles with respect to the sequence number are plotted in Fig. 7. The mean values obtained after the analysis are the following: R_1 1.1 s^{-1}, R_2 14.3 s^{-1} and NOE 0.8. Low R_2 and NOE values are observed for the regions 24–28, 76–83, 122–126 and 137–140 showing a higher mobility on the picosecond–nanosecond time scale. In contrast, the region near the mutated residue, 104–110, shows high R_2 values, suggesting a conformational exchange process on the microsecond–millisecond time scale.

Diffusion properties of StnII mutants studied by analytical ultracentrifugation

At the concentrations (0.50 mM) of StnII-R29Q and StnII-Y111N (molecular masses 19 255 and 19 223 Da, respectively) employed for NMR spectroscopy, the data obtained from equilibrium sedimentation are best fitted by a monomer ↔ dimer equilibrium. The apparent molecular masses are 29 600 Da for the StnII-R29Q variant and 24 880 Da for the StnII-Y111N variant. These data clearly indicate that under conditions used for the NMR relaxation and structural studies these proteins, especially StnII-R29Q, show some tendency to associate. A similar situation has been demonstrated previously for the wild-type protein [19].

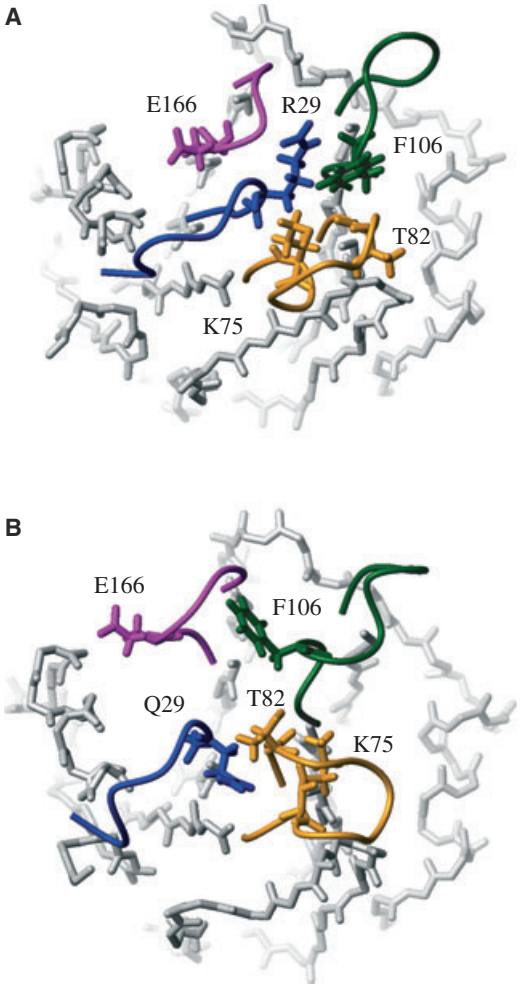

Fig. 5. Comparison of the loop regions located in the mutation face for the X-ray structure of wild-type StnII (A) and for the minimal energy structure of the StnII-R29Q mutant (B). Side chains of residues R/Q29 in loop 23–32 are in blue, K75 and T82 in loop 72–84 are in orange, F106 in loop 103–113 are in green and E166 in loop 162–168 are in red. These figures were produced with PYMOL [30].

Discussion

The three-dimensional data presented here agree with those previously reported on the basis of far UV-CD

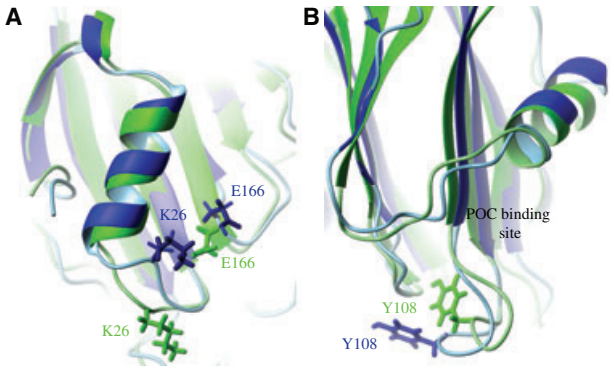

Fig. 6. Ribbon representation of the superposition of the backbone atoms of the wild-type StnII (green) and the StnII-Y111N (blue) for the N-terminal region (A) and for the membrane binding site (B). Side chains of residues that change orientation upon mutation are represented. These figures were produced using MOLMOL [29].

and IR data, showing that mutations at positions 29 and 111 do not alter the overall fold of StnII [16]. Despite the conservation of the tertiary structure and tendency to form quaternary structure, both StnII-R29Q and wild-type StnII-Y111N mutants have a highly diminished lytic activity in comparison with wild-type StnII. This decrease has been related to their low association constant for membranes [16]. However, the decrease in membrane bindings is identical, whereas the lytic activity is five times lower for StnII-Y111N than for StnII-R29Q. This significant difference led us to propose different roles in membrane lysis for Y111 and R29. The roles are revealed by the high resolution NMR studies of the structure and dynamics of these variants reported here.

The structural results presented now confirm the strategic location of R29. Its substitution by glutamine affects not only the structure and dynamics of its local environment and the four nearby loops but also the conformation of sequence stretches located near the C-terminus of the molecule. All these loops and stretches are distant along the sequence (Figs 2, 3 and 5). The NMR relaxation data show very clearly that these regions are highly dynamic in both the nanosecond–picosecond and millisecond–microsecond time scales (Fig. 3). Therefore, the decreased membrane binding observed for this variant could be related to the increased conformational freedom of these regions. Moreover, the distribution of the electrostatic potential along the surface of the protein face involved in recognizing the membrane changes significantly (Fig. 4). A dramatic loss of positive potential could affect interactions with the negatively charged phosphate groups from the phospholipid heads at the membrane surface. In this regard, it seems clear that changes on the protein surface could play a key role in targeting these proteins to the membranes as the electrostatic interactions are effective at long range. In addition, the loss of interactions due to the R29Q substitution endows

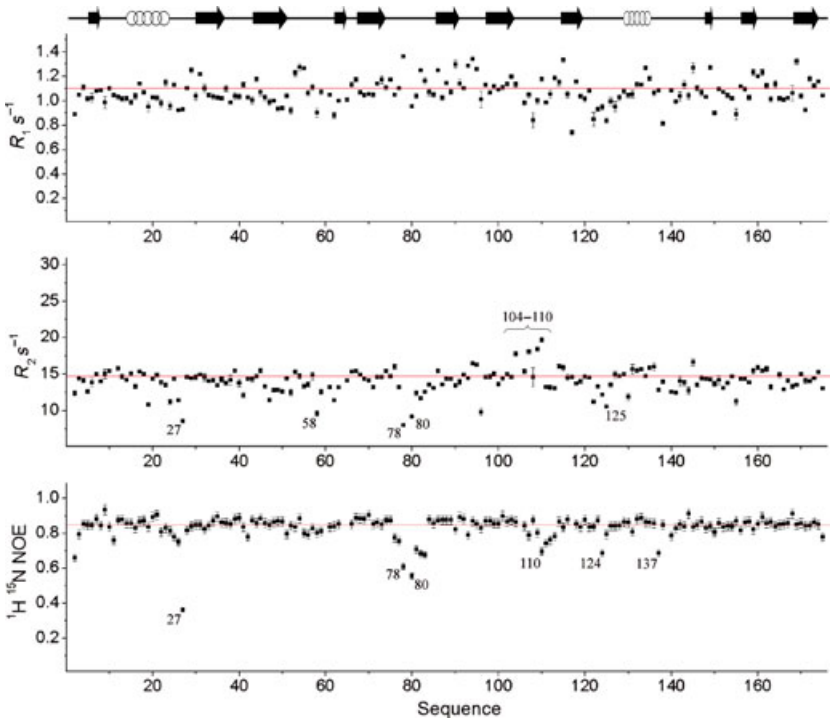

Fig. 7. Backbone heteronuclear R_1 and R_2 relaxation rates and NMR NOE relaxation data for StnII-Y111N (800 MHz, 25 °C and pH 4.0). The horizontal line represents the mean value.

the hinge region between helix-α_1 and the protein core with a dynamic flexibility not found in StnII-Y111N and most probably not present in wild-type StnII. Unfortunately wild-type StnII has not yet been studied by NMR methods and no relaxation data are available. However, according to the B-factors reported in its X-ray structure (Fig. 1) [6], this region does not show signs of important flexibility. The flexibility observed in StnII-R29Q could facilitate detachment of helix-α_1 in the mutant and explain why the R29Q mutant has a lytic activity that, although low with respect to StnII, is higher than what would be expected from its weak affinity for membranes [16]. The loss of interactions involving Arg29 when it is replaced by Gln (Fig. 5) would then facilitate the movement of this α-helix and the pore formation following the stage of initial contact.

Regarding the Y111N mutant, it is evident that the global structure and in particular the loop segments on the interacting face are very well defined and lack internal flexibility. This behaviour is in striking contrast to that observed in the R29Q mutant and the wild-type protein. Probably the hydrogen bond found in the structure of the Y111N mutant, between N111 and D107, plays an important role in rigidifying its nearby loops. Thus, according to the StnII X-ray structure and on the basis of the reported B-factors [6], loop 105–113, which comprises part of the aromatic cluster and the POC binding site, is highly dynamic in wild-type StnII (Fig. 1). In particular, the B-factors of N109 and W110 are > 80, and no density was reported for the side chain of this later amino acid. The differences between StnII and its Y111N variant clearly suggest that the Tyr at position 111, essential for membrane interaction, induces intrinsic local disorder which seems to be key for function [20].

The structural changes compromise regions that are important for membrane interaction (loop 105–113 and helix-α_2 and its surroundings) and insertion (N-terminus end and loop 25–29), as described above. Interestingly, the modifications in loop 25–29 (Fig. 2, cyan), new electrostatic interactions supplied by the K26 side chain (Fig. 6), and extension of strand-β_1 (Fig. 2C) probably contribute to rigidifying this region, hampering the detachment of helix-α_1. Therefore, Y111N represents the opposite situation to R29Q. As stated above, Y111N is less lytic than predicted from its binding affinity [16]. Thus, the decrease in lytic activity for Y111N-StnII can be explained by the additive effects of a decreased membrane affinity due to lack of the necessary local flexibility together with the long-range modifications observed along the N-terminal region, which would hamper later stages for pore formation subsequent to the initial contact with the membrane.

Observation of the dynamic properties of StnII-R29Q reveals the unexpectedly high R_2 values for the regions comprising residues 140–147 and 159–163, not located at the membrane interaction face. These stretches partially overlap the β-hairpin composed by β-strands 145–150 and 156–161 and they are rich in hydrophobic and exposed residues. In particular, the aromatic rings of Y140 and W146 have high accessible surface area (30% and 35%, respectively). To date, no specific function has yet been assigned to this region of the actinoporin structure. Considering the results mentioned above, it is tempting to speculate that the conformational processes affecting these residues could be involved in other types of molecular interactions apart from those involving lipid binding and pore formation. Accordingly, the hydrophobic moieties of these segments could contribute to oligomerization as detected by the ultracentrifuge experiments.

In summary, the results reported here permit us to corroborate and extend the model for actinoporin membrane binding and lysis. In addition to confirming roles for the hinge loop flexibility for helix-α_1 membrane penetration, the results support the importance of a network of electrostatic interactions, anchored by R29, in the first stage of membrane binding. Y111 induces a necessary disorder in exposed hydrophobic side chains that promotes their interaction with the membrane.

Materials and methods

Expression and purification of StnII-R29Q and StnII-Y111N mutants

The unlabelled StnII-R29Q and the double uniformly labelled $^{13}C/^{15}N$ StnII-R29Q and $^{13}C/^{15}N$ StnII-Y111N samples were produced using an *Escherichia coli* expression system following a previously described protocol [21–23]. For the labelled forms, cells were grown in an M9 minimal medium with $^{15}NH_4Cl$ (1 g·L^{-1}) and $^{13}C_6$-glucose (4 g·L^{-1}) as the sole nitrogen and carbon sources. Protein purification was achieved by ion exchange chromatography on CM52 equilibrated in 50 mM Tris/HCl, pH 6.8 for StnII-R29Q or pH 7.8 for StnII-Y111N. The homogeneity of all protein samples used was confirmed by SDS/PAGE and amino acid analysis.

NMR sample preparation

Typically samples contained up to 0.5 mM of protein and were prepared in both 90% H_2O/10% D_2O and D_2O at

pH 4.0 (uncorrected for deuterium isotope effects). Sodium-4,4-dimethyl-4-silapentane-1-sulfonate was used as internal ^{1}H chemical shift reference.

NMR structure calculation

All the NMR spectra were recorded in a Bruker AV-800 instrument equipped with cryoprobe and field gradients. All data were acquired and processed with TOPSPIN (version 1.3) (Bruker, Rheinstetten, Germany) at 25 °C. Spectral assignment was done using sets of standard two-dimensional and three-dimensional experiments as reported previously [22,23]. Three-dimensional ^{15}N-NOESY-HSQC and ^{13}C-NOESY-HSQC spectra with 50 ms mixing times were recorded for both proteins. In addition, two-dimensional ^{1}H-^{1}H NOESY spectra with 80 ms mixing time in 90% H_2O/10% D_2O and D_2O solutions were recorded with the unlabelled StnII-R29Q sample. The spectral analysis was performed with the program SPARKY (version 3.1) [24] on the bases of the published assignments [22,23]. The structure calculation of the StnII-R29Q and StnII-Y111N variants was performed with CYANA [25] using the automatic NOE assignment facility combined with lists of manually assigned NOEs. NOE intensities were calibrated with CYANA and used as upper distance limit constraints in the calculations. Moreover, backbone dihedral angle constraints were determined from chemical shift values using TALOS [26] and incorporated into the structure calculation protocol. Initially, 100 conformers were generated that were forced to satisfy the experimental data during a standard automatic CYANA protocol based on simulated annealing using torsion angle dynamics. The 20 conformers with the lowest final CYANA target function values were selected and subjected to 2000 steps of energy minimization using the generalized Born continuum solvation model implemented in AMBER9 [27] with a non-bonded cutoff of 10 Å. The final structure quality was checked with PROCHECK-NMR [28]. The structures have no representative experimental distance violations > 0.4 Å or dihedral angle violations $> 5°$. Coordinates for the final set of 20 structures have been deposited in the Protein Data Bank database with accession number 2KS3 for StnII-R29Q and 2L2B for StnII-Y111N. The programs MOLMOL [29] and PYMOL [30] were used for molecular display and structure analysis.

NMR dynamics

All NMR relaxation experiments were carried out in the same conditions as described above. Conventional ^{15}N heteronuclear relaxation rates R_1, R_2 and NOE data were determined (Fig. S1). To this end, a series of two-dimensional heteronuclear correlated spectra using a sensitivity enhanced gradient pulse scheme [31] were recorded. The relaxation delay times were set as follows: for R_1, 5, 50, 150, 300, 600, 800, 1000 and 1200 ms; and for R_2, 15.6, 31.3, 46.8, 62.5, 78.2, 93, 109.4 and 125 ms. The relaxation rate constants R_1 and R_2 were obtained from the exponential fits of the measured cross-peak intensities. The uncertainty was taken as the error in the fit of the decay function. For the NOE measurement, the experiments with and without proton saturation were acquired simultaneously in an interleaved manner with a recycling delay of 5 s and were split during processing into separate spectra for analysis. The values for the heteronuclear NOEs were obtained from the ratio intensities of the resonances with and without saturation. Here, the uncertainty was estimated to be about 5%.

Analytical ultracentrifugation

Ultracentrifugation was performed on a Beckman-Coulter Optima XL-1 analytical ultracentrifuge at 20 °C. The sample solutions were those used in NMR in water at pH 4.0. Both equilibrium sedimentation and sedimentation velocity (final velocity 24 000 r.p.m.) experiments were conducted. The HETEROANALYSIS program [32] was used to analyse the results.

Acknowledgements

This work was supported by projects CTQ2008-00080/BQU and BFU2009-10185 from the Spanish Ministerio de Ciencia e Innovación. We thank Dr D.V. Laurents for critical comments on the manuscript.

References

1 Macek P (1992) Polypeptide cytolytic toxins from sea anemones (*Actiniaria*). *FEMS Microbiol Immunol* **5**, 121–129.
2 Anderluh G & Macek P (2002) Cytolytic peptide and protein toxins from sea anemones (*Anthozoa: Actiniaria*). *Toxicon* **40**, 111–124.
3 Alegre-Cebollada J, Oñaderra M, Gavilanes JG & Martínez-del-Pozo AM (2007) Sea anemone actinoporins: the transition from a folded soluble state to a functionally active membrane-bound oligomeric pore. *Curr Protein Pept Sci* **8**, 558–572.
4 Anderluh G, Dalla Serra M, Viero G, Guella G, Macek P & Menestrina G (2003) Pore formation by equinatoxin II, a eukaryotic protein toxin, occurs by induction of nonlamellar lipid structures. *J Biol Chem* **278**, 45216–45223.
5 Bakrac B & Anderluh G (2010) Molecular mechanism of sphingomyelin-specific membrane binding and pore formation by actinoporins. *Adv Exp Med Biol* **677**, 106–115.
6 Mancheño JM, Martín-Benito J, Martínez-Ripoll M, Gavilanes JG & Hermoso JA (2003) Crystal and

electron microscopy structures of sticholysin II actinoporin reveal insights into the mechanism of membrane pore formation. *Structure* **11**, 1319–1328.
7 Athanasiadis A, Anderluh G, Macek P & Turk D (2001) Crystal structure of the soluble form of equinatoxin II, a pore-forming toxin from the sea anemone *Actinia equina*. *Structure* **9**, 341–346.
8 Hinds MG, Zhang W, Anderluh G, Hansen PE & Norton RS (2002) Solution structure of the eukaryotic pore-forming cytolysin equinatoxin II: implications for pore formation. *J Mol Biol* **315**, 1219–1229.
9 Castrillo I, Araujo NA, Alegre-Cebollada J, Gavilanes JG, Martínez-del-Pozo A & Bruix M (2010) Specific interactions of sticholysin I with model membranes: an NMR study. *Proteins* **78**, 1959–1970.
10 Anderluh G, Razpotnik A, Podlesek Z, Macek P, Separovic F & Norton RS (2005) Interaction of the eukaryotic pore-forming cytolysin equinatoxin II with model membranes: 19F NMR studies. *J Mol Biol* **347**, 27–39.
11 Bakrac B, Gutierrez-Aguirre I, Podlesek Z, Sonnen AF, Gilbert RJ, Macek P, Lakey JH & Anderluh G (2008) Molecular determinants of sphingomyelin specificity of a eukaryotic pore-forming toxin. *J Biol Chem* **283**, 18665–18677.
12 Kristan K, Viero G, Macek P, Dalla Serra M & Anderluh G (2007) The equinatoxin N-terminus is transferred across planar lipid membranes and helps to stabilize the transmembrane pore. *FEBS J* **274**, 539–550.
13 Kristan KC, Viero G, Dalla Serra M, Macek P & Anderluh G (2009) Molecular mechanism of pore formation by actinoporins. *Toxicon* **54**, 1125–1134.
14 Mechaly AE, Bellomio A, Gil-Carton D, Morante K, Valle M, González-Mañas JM & Guerín DM (2011) Structural insights into the oligomerization and architecture of eukaryotic membrane pore-forming toxins. *Structure* **19**, 181–191.
15 Alegre-Cebollada J, Lacadena V, Oñaderra M, Mancheño JM, Gavilanes JG & Martínez-del-Pozo AM (2004) Phenotypic selection and characterization of randomly produced non-haemolytic mutants of the toxic sea anemone protein sticholysin II. *FEBS Lett* **575**, 14–18.
16 Alegre-Cebollada J, Cunietti M, Herrero-Galán E, Gavilanes JG & Martínez-del-Pozo A (2008) Calorimetric scrutiny of lipid binding by sticholysin II toxin mutants. *J Mol Biol* **382**, 920–930.
17 Monastyrnaya M, Leychenko E, Isaeva M, Likhatskaya G, Zelepuga E, Kostina E, Trifonov E, Nurminski E & Kozlovskaya E (2010) Actinoporins from the sea anemones, tropical *Radianthus macrodactylus* and northern *Oulactis orientalis*: comparative analysis of structure–function relationships. *Toxicon* **56**, 1299–1314.
18 Uechi G, Toma H, Arakawa T & Sato Y (2010) Molecular characterization on the genome structure of hemolysin toxin isoforms isolated from sea anemone *Actineria villosa* and *Phyllodiscus semoni*. *Toxicon* **56**, 1470–1476.
19 de los Rios V, Mancheño JM, Martinez del Pozo A, Alfonso C, Rivas G, Oñaderra M & Gavilanes JG (1999) Sticholysin II, a cytolysin from the sea anemone *Stichodactyla helianthus*, is a monomer-tetramer associating protein. *FEBS Lett* **455**, 27–30.
20 Zidek L, Novotny MV & Stone MJ (1999) Increased protein backbone conformational entropy upon hydrophobic ligand binding. *Nat Struct Biol* **6**, 1118–1121.
21 Alegre-Cebollada J, Clementi G, Cunietti M, Porres C, Oñaderra M, Gavilanes JG & Martínez del Pozo A (2007) Silent mutations at the 5′-end of the cDNA of actinoporins from the sea anemone *Stichodactyla helianthus* allow their heterologous overproduction in *Escherichia coli*. *J Biotechnol* **127**, 211–221.
22 Pardo-Cea MA, Alegre-Cebollada J, Martinez-del-Pozo A, Gavilanes JG & Bruix M (2010) ^{1}H, ^{13}C, and ^{15}N NMR assignments of StnII-Y111N, a highly impaired mutant of the sea anemone actinoporin Sticholysin II. *Biomol NMR Assign* **4**, 69–72.
23 Castrillo I, Alegre-Cebollada J, Martinez-del-Pozo A, Gavilanes JG & Bruix M (2009) ^{1}H, ^{13}C, and ^{15}N NMR assignments of StnII-R29Q, a defective lipid binding mutant of the sea anemone actinoporin Sticholysin II. *Biomol NMR Assign* **3**, 239–241.
24 Goddard TD & Kneller DG (2005) *SPARKY 3*. University of California, San Francisco, CA.
25 Güntert P (2004) Automated NMR structure calculation with CYANA. *Methods Mol Biol* **278**, 353–378.
26 Cornilescu G, Delaglio F & Bax A (1999) Protein backbone angle restraints from searching a database for chemical shift and sequence homology. *J Biomol NMR* **13**, 289–302.
27 Case DA, Cheatham TE III, Darden T, Gohlke H, Luo R, Merz KM Jr, Onufriev A, Simmerling C, Wang B & Woods RJ (2005) The Amber biomolecular simulation programs. *J Comput Chem* **26**, 1668–1688.
28 Laskowski RA, Rullmann JAC, MacArthur MW, Kaptein R & Thornton JM (1996) AQUA and PROCHECK-NMR: programs for checking the quality of protein structures solved by NMR. *J Biomol NMR* **8**, 477–486.
29 Koradi R, Billeter M & Wüthrich K (1996) MOLMOL: a program for display and analysis of macromolecular structures. *J Mol Graph* **14**, 29–32.
30 DeLano WL (2006) The PyMol molecular graphics system. Version 1.3, Schrödinger, LLC. San Francisco, CA.
31 Farrow NA, Muhandiram R, Singer AU, Pascal SM, Kay CM, Gish G, Shoelson SE, Pawson T, Forman-Kay JD & Kay LE (1994) Backbone dynamics of a free and phosphopeptide-complexed Src homology 2 domain studied by ^{15}N NMR relaxation. *Biochemistry* **33**, 5984–6003.

32 Cole J & Lary J (2009) *HeteroAnalysis*. Analytical Ultracentrifugation Facility, Bioservices Center, University of Connecticut, Storrs, CT.

Supporting information

The following supplementary material is available:
Fig. S1. Heteronuclear ^{1}H–^{15}N NOE spectra of StnII-Y111N variant. Both NMR spectra with and without saturation are represented. Signals are labelled with the one letter amino acid code and the sequence number.

This supplementary material can be found in the online version of this article.

Please note: As a service to our authors and readers, this journal provides supporting information supplied by the authors. Such materials are peer-reviewed and may be re-organized for online delivery, but are not copy-edited or typeset. Technical support issues arising from supporting information (other than missing files) should be addressed to the authors.